

Supplementary Information: Redox-dependent
Franck-Condon blockade and avalanche transport in a
graphene-fullerene single-molecule transistor

December 1, 2015

Contents

| | | |
|----------|---|-----------|
| 1 | Experimental details | 3 |
| 1.1 | Synthesis of the fullerene-pyrene bisadducts | 3 |
| 1.2 | Mass spectroscopy | 3 |
| 1.3 | Raman spectroscopy | 3 |
| 1.4 | Rate equation model | 5 |
| 1.5 | Determining peak positions, excited state energies, t_0 , I_{step}^n and λ | 6 |
| 1.6 | Magnetic field measurements | 9 |
| 1.7 | Charge stability diagrams of device B and C | 9 |
| 1.8 | Temperature dependence measurements | 9 |
| 1.9 | Current noise measurements and Hidden Markov Model | 10 |
| 2 | DFT Calculations | 11 |
| 2.1 | Methods | 11 |
| 2.2 | Molecular geometry | 13 |
| 2.3 | Local density of states | 13 |
| 2.4 | Device geometry | 14 |
| 2.5 | Electron transport | 15 |
| 2.6 | Vibrational modes of the cis-3 and cis-2 isomers. | 15 |

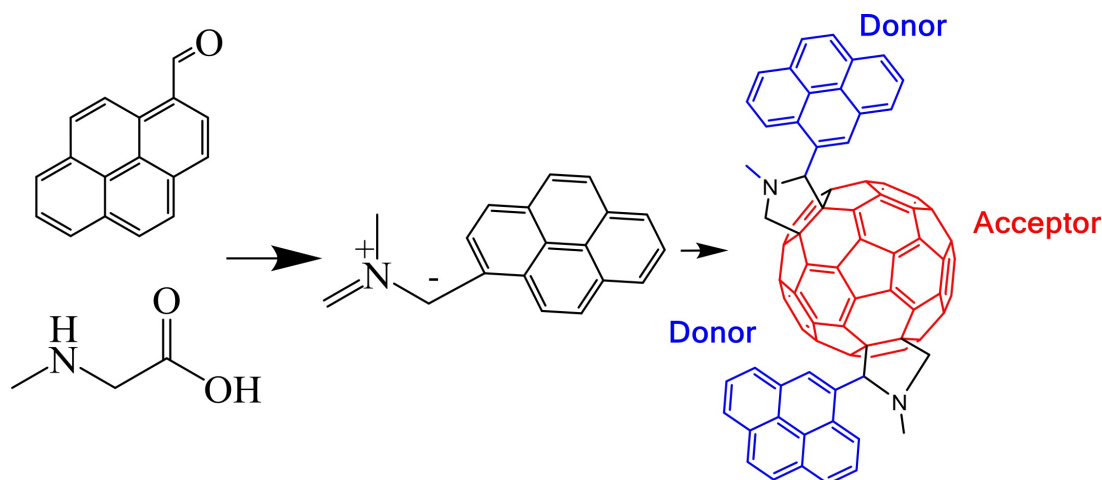


Figure S1: Schematic representation of the 1,3 dipolar cycloaddition reaction.

1 Experimental details

1.1 Synthesis of the fullerene-pyrene bisadducts

Bisadducts of C_{60} with pyrene anchor groups were synthesized through the 1,3 dipolar cycloaddition on the surface of C_{60} . In a typical experiment 1-pyrene carboxaldehyde (4.83 mg-0.021 mmol-Sigma Aldrich 99 %), N-methylglycine (sarcosine, 2.41 mg-0.027 mmol-Sigma Aldrich 98 %) and C_{60} (5.73 mg-0.008 mmol-MER Corporation 98 %) were dissolved in 9 ml of toluene. The reaction proceeded under continuous nitrogen flow at 110 °C. The purification of the products took place through HPLC chromatography using a Buckyprep M silica column, 20 × 250 mm. Toluene was used as the eluent phase and the flow rate was 16 ml/min.

1.2 Mass spectroscopy

Matrix-assisted laser-desorption ionization time-of-flight mass spectra (MALDI-TOF MS) were obtained from a Bruker MALDI-TOF spectrometer using trans-2-[3-(4-tert-Butylphenyl)-2-methyl-2-propenylidene] malononitrile (DCTB) and dithranol as a matrix with positive or negative ionization modes. Figure S2 shows the mass spectroscopy of the C_{60} bisadduct.

1.3 Raman spectroscopy

In Figure S3 we present the Raman spectra for the bis adducts in comparison with the pristine C_{60} under 532 nm laser excitation. All the Raman active vibrational modes are indicated above each peak. We also present a magnification of the high frequency pentagonal pinch $A_g(2)$ Raman mode that is blue shifted in the bis adducts compared to the pristine C_{60} in a similar manner with other exohedrally functionalized or polymerized fullerenes.[1, 2]

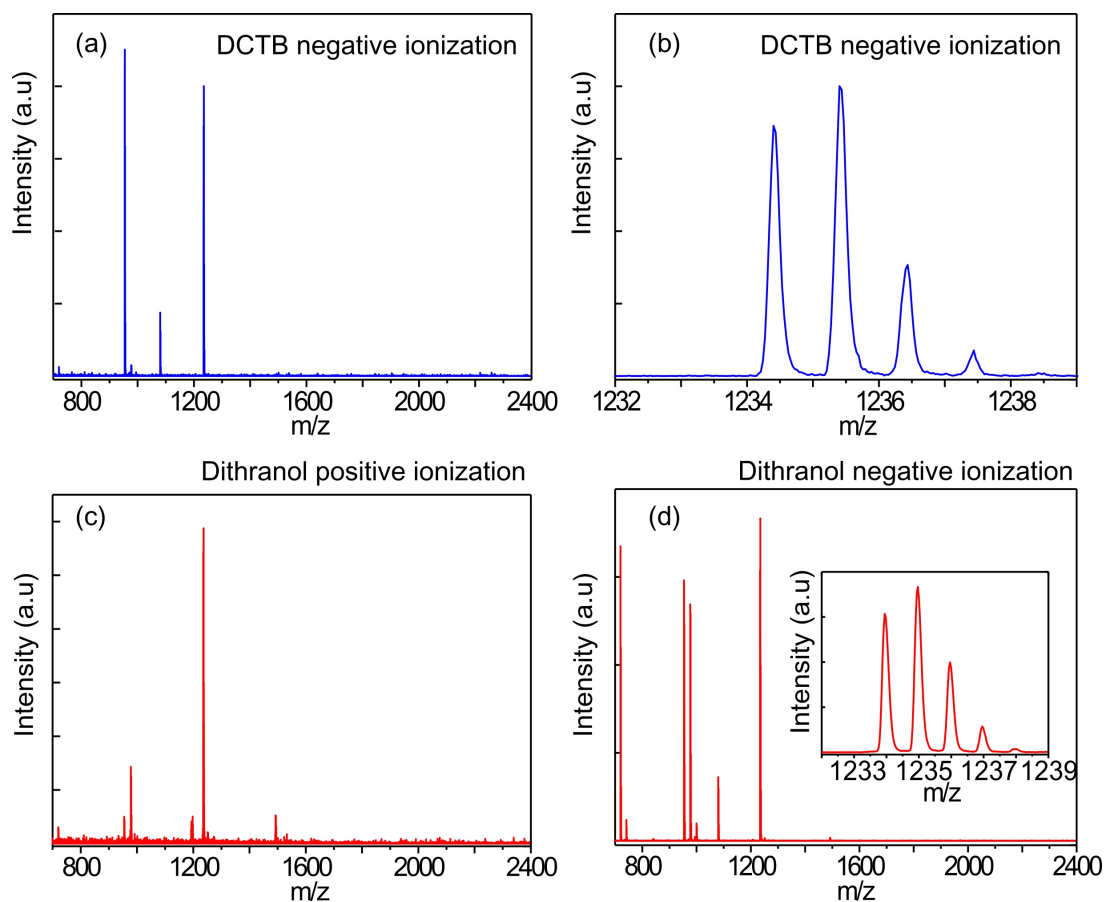


Figure S2: Mass spectroscopy of C_{60} bisadduct. (a) DCTB as matrix, negative ionization. The sample fragments in the monoadduct ($m/z \approx 977$). (b) Magnification of the bisadduct peak with the characteristic isotopic distribution. (c) Dithranol as matrix with positive ionization. The fragmentation is much less pronounced. (d) Dithranol as matrix with negative ionization. The fragmentation leads to pyrene monoadducts and pristine C_{60} .

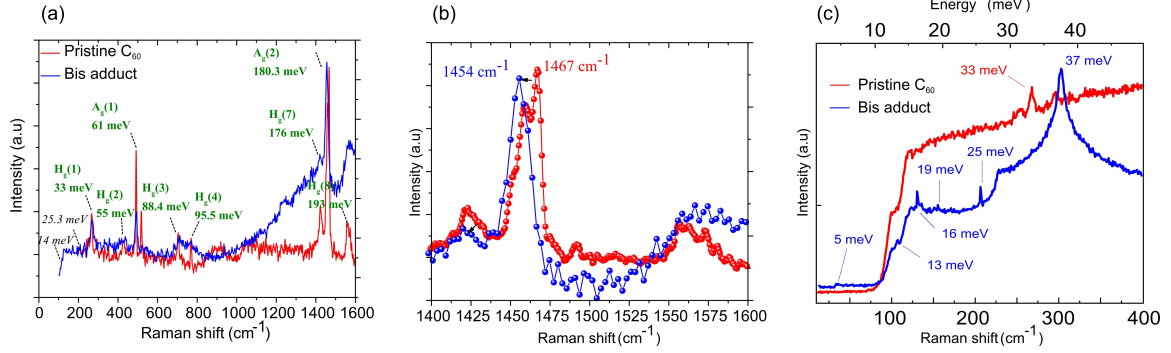


Figure S3: (a) Raman spectrum of the pristine C_{60} (red) and the bisadducts (blue) on gold coated glass substrate recorded under 532 nm laser excitation. The symmetry point groups are indicated above each peak. (b) Magnification of the $A_g(2)$ Raman mode that is blue shifted in the bisadducts compared to pristine C_{60} . (c) Low energy Raman spectra of the pristine C_{60} (red) and the bisadducts (blue) on gold coated silicon substrate showing the modes also observed in transport spectroscopy. The 37 meV peak is due to the silicon background.

1.4 Rate equation model

The model considered has been extensively discussed in [3, 4]. Here we review the pertinent points. The rate equations determine the molecular occupation probabilities P_q^n for charge state n and q vibrons, as in (1).

$$\frac{dP_q^n}{dt} = \sum_{n', q'} [P_{q'}^{n'} W_{q' \rightarrow q}^{n' \rightarrow n} - P_q^n W_{q \rightarrow q'}^{n \rightarrow n'}] - \frac{1}{\tau} [P_q^n - P_q^{eq} \sum_{q'} P_q^n] \quad (1)$$

P_q^{eq} denotes the equilibrium vibron distribution with a relaxation time τ and $W_{q \rightarrow q'}^{n \rightarrow n'}$ denotes the total rate for a transition from $|n, q\rangle$ to $|n', q'\rangle$.

$$W_{q \rightarrow q'}^{n \rightarrow (n+1)} = \sum_{a=L,R} [f_a(E_{q'}^{(n+1)} - E_q^n)] \Gamma_{q \rightarrow q'; a}^{n \rightarrow (n+1)}, \quad (2)$$

$$W_{q \rightarrow q'}^{n \rightarrow (n-1)} = \sum_{a=L,R} [1 - f_a(E_q^n - E_{q'}^{(n-1)})] \Gamma_{q \rightarrow q'; a}^{n \rightarrow (n-1)}, \quad (3)$$

where f_a is the Fermi factor and the bare transition rates Γ are calculated from Fermi's golden rule.

$$\Gamma_{q \rightarrow q'; a}^{n \rightarrow (n+1)} = s^{n \rightarrow (n+1)} \frac{2\pi}{\hbar} \rho_a(E_q^n - E_{q'}^{(n+1)}) |M_{q \rightarrow q'; a}^{n \rightarrow (n+1)}|^2, \quad (4)$$

$$\Gamma_{q \rightarrow q'; a}^{n \rightarrow (n-1)} = s^{n \rightarrow (n-1)} \frac{2\pi}{\hbar} \rho_a(E_q^n - E_{q'}^{(n-1)}) |M_{q \rightarrow q'; a}^{n \rightarrow (n-1)}|^2. \quad (5)$$

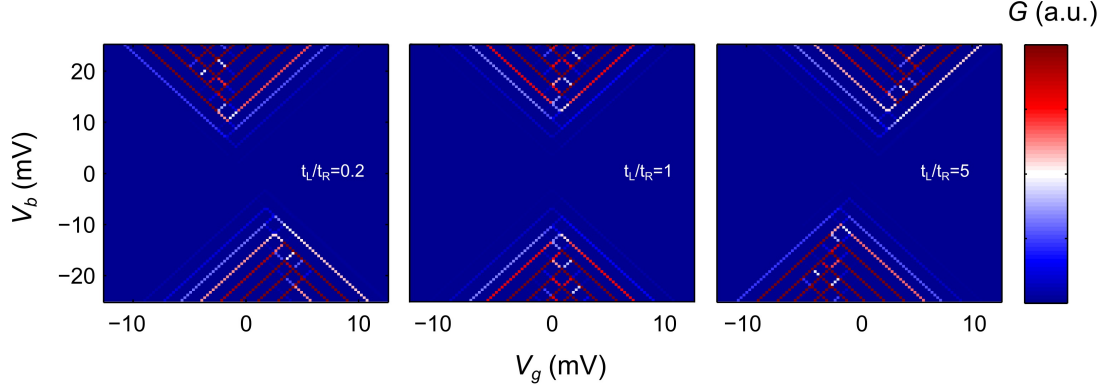


Figure S4: Simulated conductance stability diagrams using the experimentally obtained value of $\hbar\omega = 1.7$ meV and $t_L/t_R = 0.2$ (a), 1 (b) and 5 (c).

Here, ρ_a denotes the density of states in lead a , assumed in our calculations to be constant for both leads, $M_{q \rightarrow q'; a}^{n \rightarrow (n \pm 1)}$ denotes the FC matrix elements and $s^{n \rightarrow m}$ the spin factor such that for sequential tunnelling and assuming twofold degeneracy they are

$$s^{1 \rightarrow 0} = s^{1 \rightarrow 2} = 1, s^{0 \rightarrow 1} = s^{2 \rightarrow 1} = 2. \quad (6)$$

The matrix elements $M_{q \rightarrow q'; a}^{n \rightarrow (n \pm 1)}$ defined for vibrations are

$$M_{q \rightarrow q'; a}^{n \rightarrow (n \pm 1)} = t_0 (q_1! / q_2!)^{1/2} \times \lambda^{q_2 - q_1} e^{-\lambda^2/2} \quad (7)$$

where $q_1 = \min\{q, q'\}$ and $q_2 = \max\{q, q'\}$.

Figure S4 shows the simulated conductance stability diagrams for different ratios of t_L/t_R for comparison.

1.5 Determining peak positions, excited state energies, t_0 , I_{step}^n and λ

We extract the energies of the vibrational states in Figure S5a by first determining the slopes of the Coulomb diamond edges. The white circles indicate the maximum conductance over a small bias window at fixed gate voltages. A typical bias window is indicated by the vertical white line. We next extract the slopes using straight line fits (red line) to the points indicated by the white circles. The slopes are then used to determine the area (yellow boxes) over which we average the conductance. The averaged conductance as a function of the energy are shown in Figure S5b (positive bias) and S5c (negative bias). The energy axis is scaled by offsetting the first conductance peak to zero energy. We can then determine the energies of the excited state lines.

To determine $\hbar\omega$ we use the IV trace at $V_g = 10.85$ V (Figure S6a) which shows a series of steps due to vibron transitions. The current step is fitted to a thermally broadened Lorentzian,

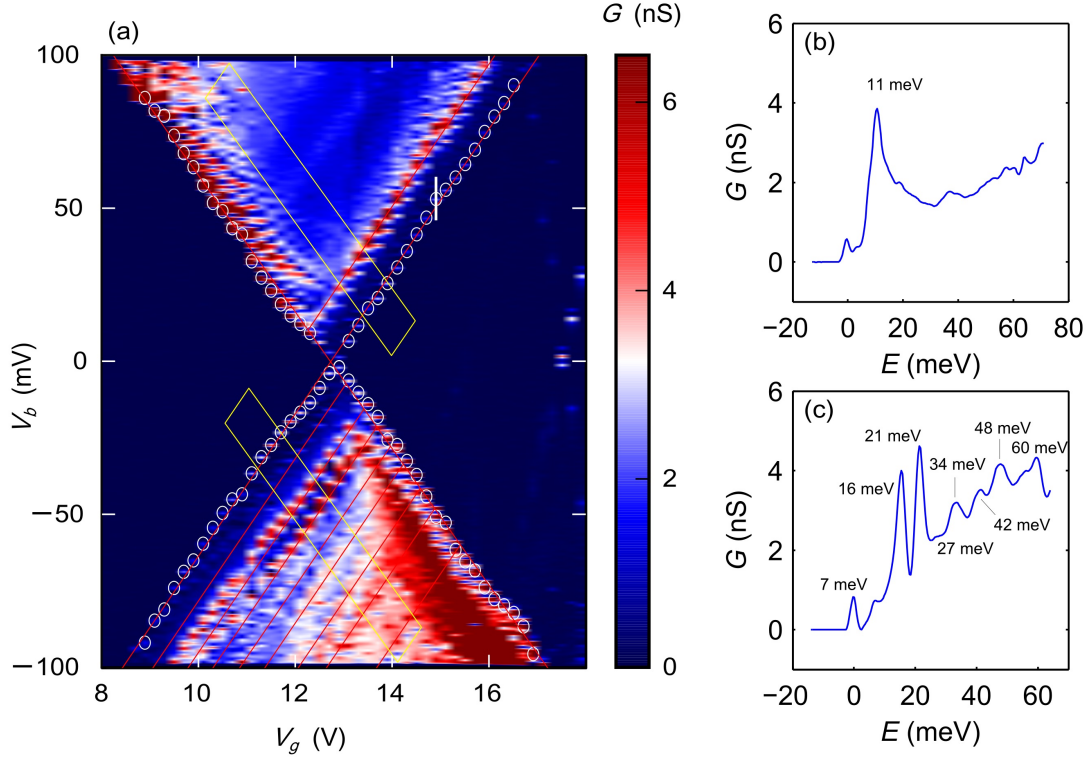


Figure S5: (a) Conductance stability diagram of charge transition P3 of device A at 20 mK. The white circles indicate the maximum conductance over a small bias range, indicated by the white vertical line. The points indicated by the white circles are then fitted to a straight line to determine the slopes of the Coulomb diamond edges (red line). The yellow box, determined by the slope of the Coulomb diamond edges, indicates the area for which the conductance is averaged. (b) The averaged conductance as a function of energy for positive bias and (c) negative bias.

as in (8).[5, 6]

$$I^n = I_{\text{step}}^n \int \frac{1}{(e^{\alpha V_g - E_{\text{res}} - E}/kT + 1)} \frac{ht_0/2}{(ht_0/2)^2 + E^2} dE \quad (8)$$

where I_{step}^n is the amplitude, V_g the gate voltage, α the gate coupling, E_{res} is the resonance energy, t_0 is the molecule-electrode tunnel coupling, and E is the energy over which the integral is taken (Figure S6b). We fit $I - V$ at different V_g to determine the peak positions V_0 , t_0 and I_{step}^n as a function of the current steps n , as in Figure S6c. The energy of the excitations are then extracted from the intersection of the excited state lines with the Coulomb diamond edges.

To determine λ , we first extract the five current step heights I_{step}^n from the stability diagram of P3 at $V_g = 10.85$ V. I_{step}^n is then fitted to a set of current heights generated using the rate equation model, as in Figure S6d.[3, 4]

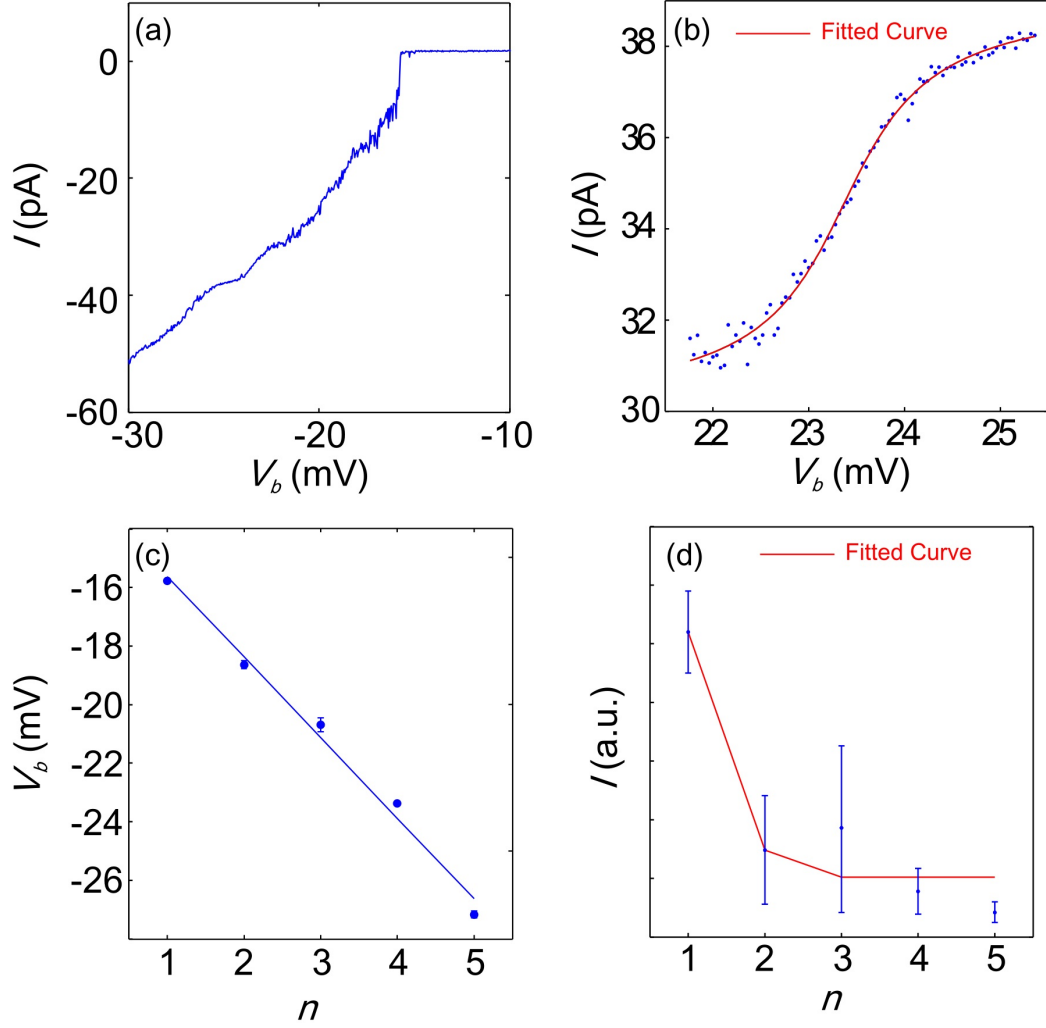


Figure S6: (a) IV trace at $V_g = 10.85$ V, showing current steps from vibron transitions. (b) Typical fit of the current steps to a thermally broadened Lorentzian to extract $t_0 = 1.36$ meV and $V_0 = 23.4$ mV. (c) Fitted peak positions V_0 as a function of the current steps n . The straight line fit yields a vibrational quantum of $\hbar\omega = 1.7$ meV. (d) I_{step} is fitted to the current step heights generated using the rate equation model to extract $\lambda = 3$.

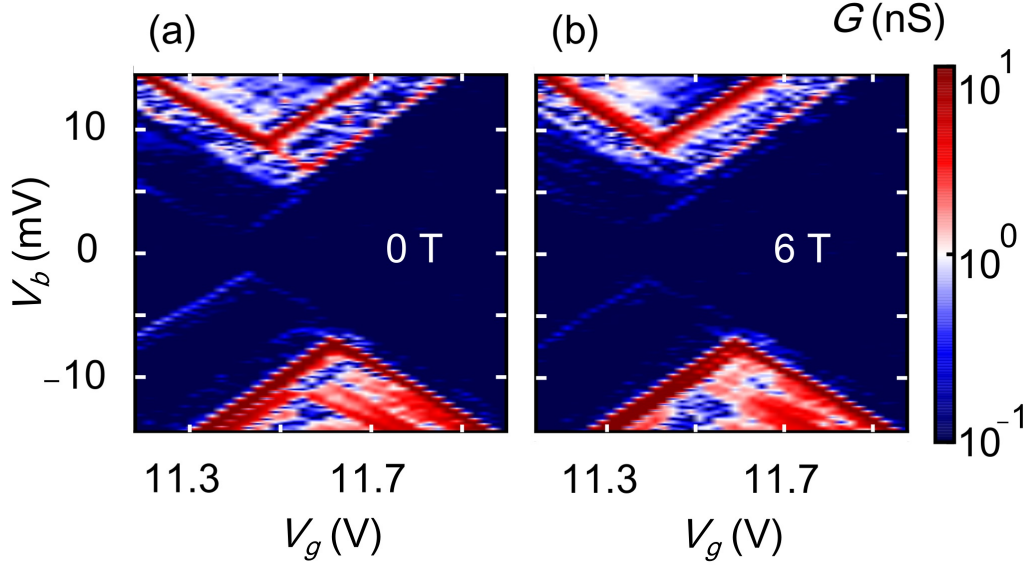


Figure S7: Magnetic field dependence. Charge stability diagrams of P3 at 0 T (a) and 6 T (b). The FC gap has no magnetic dependence.

1.6 Magnetic field measurements

An in-plane magnetic field of 6 T was applied to the device (Figure S7). No change to the low bias current suppression was observed, suggesting a non-magnetic origin for the gap.

1.7 Charge stability diagrams of device B and C

Figure S8a shows device B measured at 20 mK. The low energy excitations similarly observed in device A is present. However, there is no FC gap, suggesting a smaller λ . In device C (Figure S8b, measured at 20 mK), the FC gap is present. Inelastic co-tunnelling lines running horizontal with the gate axis can be observed. At 4 K, the FC gap is lifted, similar to device A.

1.8 Temperature dependence measurements

Transitions due to vibron absorption are described by Bose-Einstein statistics, such that $I_{\text{step}}^0 \propto 1/k_B T \times 1/(\exp(\hbar\omega/k_B T) - 1)$. [7] We extract and fit the temperature dependence of I_{step}^0 at $V_g = 7$ V and $V_b = 7.2$ mV in Figure 3c of the maintext and obtained a value of $\hbar\omega = 1.7$ meV, accordant with our experimentally obtained value. We extract the peak heights by fitting the current steps for different temperatures as described in section 1.5. The gate shifts were managed by fitting the IV traces for different temperatures where the current steps occur at the same bias. Figure S9a shows the fit (black curve) to our data. For comparison, the curves for a value

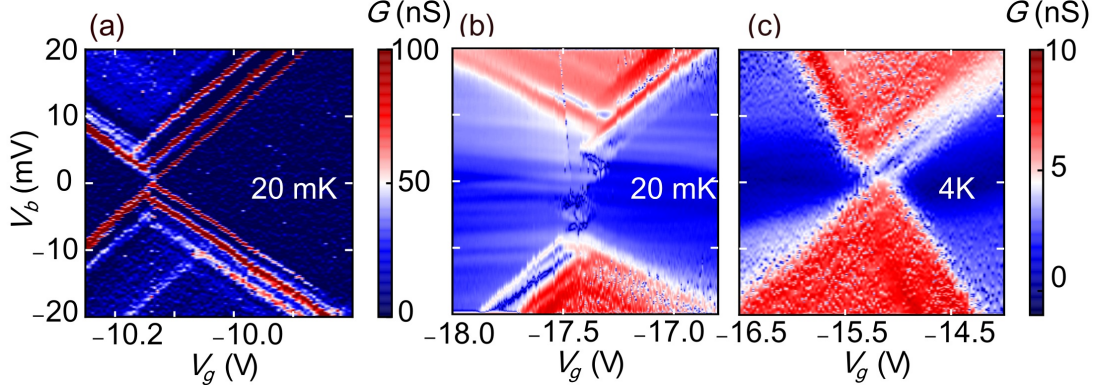


Figure S8: Charge stability diagrams of device B at 20 mK (a) and device C at 20 mK(b) and 4 K (c). The 2 meV lines seen in device A is present in this device. However, there is no FC gap, suggesting a smaller λ . The FC gap is visible in device C. Inelastic co-tunnelling lines are seen running horizontal with the gate axis. At 4 K, the FC gap is lifted.

of $\hbar\omega = 0.17$ meV (green) and 17 meV (red). Figure S9b shows the normalised curves over a larger temperature range.

1.9 Current noise measurements and Hidden Markov Model

The current-time characteristics is taken with a sampling frequency of 100 kHz using an oscilloscope. The noise power density is then determined using the following definition with a Gaussian window.

$$S(\omega) = \int_{-\infty}^{\infty} dt e^{i\omega t} \langle \delta I(t + t') \delta I(t') \rangle_{t'}. \quad (9)$$

$S(\omega)$ for $V_b = 9, 12$ and 14 mV is shown in Figure S10a. The cutoff frequency occurs at ~ 100 Hz due to the bandwidth limit of our current amplifier.

The Fano factor $F = S/2e\langle I \rangle$ for the excess noise $S(0) - S(0)_{V_b=0}$ indicates the deviation from Poissonian noise, where $F = 1$. $\langle I \rangle$ denotes the average current. Sequential tunnelling is characterized by $0.5 < F < 1$ depending on the ratio of t_L and t_R [8]. Transport can also proceed via higher order co-tunnelling processes, such as inelastic co-tunnelling, which leads to super-Poissonian noise with F up to 8.[9] In contrast, electron avalanche-like transport is predicted in systems with strong electron-vibron coupling and weak vibron relaxation.[4] We first calculate the noise power density from our current-time traces using equation (1), and then determine the zero frequency Fano factors using $F = S/2e\langle I \rangle$ for the excess noise.

We use the software package SMART: Single Molecule Analysis Research Tool to fit the current-time traces to Hidden Markov Models (HMM) using a simple two state system as illustrated in Figure S10b.[10] For each state in the model the software determines the probability

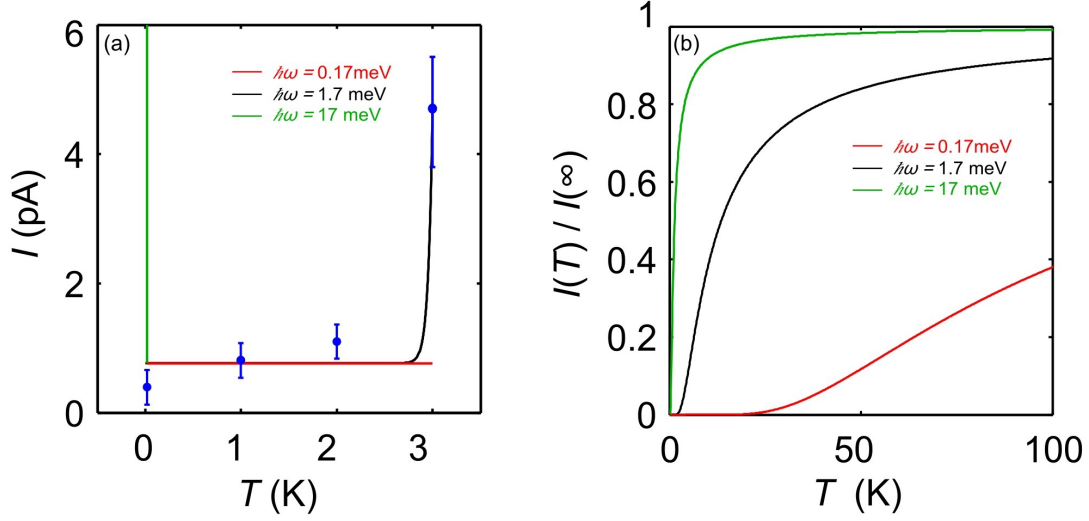


Figure S9: (a) Fit of the current steps to the Bose-Einstein distribution, yielding $\hbar\omega = 1.7$ meV (black curve). For comparison, the curves for $\hbar\omega = 0.17$ meV (green) and 17 meV (red) are shown. (b) Normalised curves over a larger temperature range. The error bars for the points at 20 mK, 1 K and 2 K are represented by the 95% confidence intervals as determined by the root mean square of the noise level

at each time point in the trace; a state probability close to 1 indicates a high probability that the state is occupied. This allows the rate constants k_{ij} , the rate of a transition from state i to j , to be determined. A combined kinetic and noise model is fit to each trace and the parameters for the models are determined using maximum likelihood estimation. A typical fit is shown in Figure S10c. The full current-time trace, over which we perform the HMM fit, was measured for 20 s with a 100 kHz sampling rate. The escape and return rates are determined using 14 current traces extending over the bias range over which avalanche transport occurs. The HMM fit gives the value of k_{ij} in units or per point, which are then multiplied by the conversion factor of 2 million points per 20 s.

The high current in Figure 5b in the maintext corresponds to the $0 \leftrightarrow 1$ transition such that $I_{0 \leftrightarrow 1} = e \frac{dN}{dt}$, where e is the electron charge and $\frac{dN}{dt}$ is the tunnelling rate corresponding to a transition probability of 1. The transition probability associated with an escape rate $1/\tau_e$ of $15 \pm 2 \text{ s}^{-1}$ is $1/\tau_e \frac{dN}{dt}$, which corresponds to $|M_{0 \rightarrow 1}|^2$ for $\lambda = 4$.

2 DFT Calculations

2.1 Methods

The Dynamical matrix is defined as:

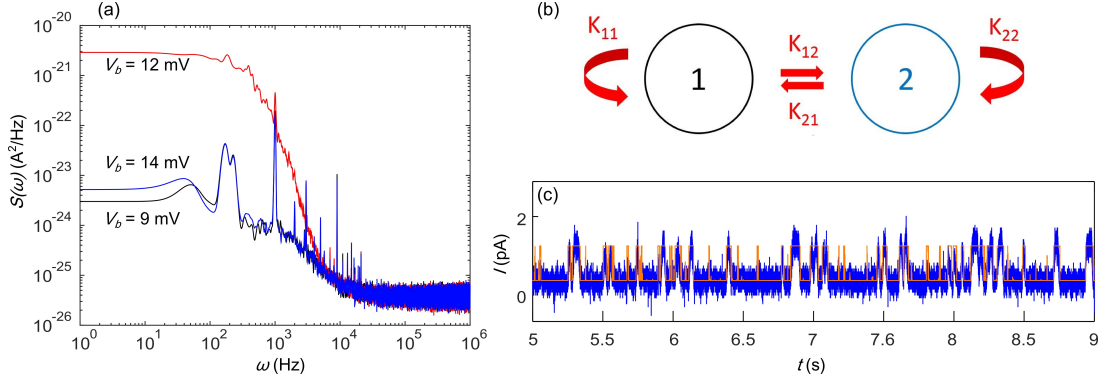


Figure S10: (a) Noise power density $S(\omega)$ for $V_b = 9, 12$ and 14 mV. (b) Schematic of a two state system described by the HMM model, where the rate constants k_{ij} describes the rate of a transition from state i to j . (c) The HMM fit (orange curve) shown for a longer current-time trace than Figure 5 in the maintext. The HMM fits are performed for the full current-time traces taken for 20 s at a sampling frequency of 100 kHz.

$$D_{ij} = \frac{K_{ij}^{qq'}}{M_{ij}} \quad (10)$$

where K for $i \neq j$ are obtained from finite differences.

$$K_{ij}^{qq'} = \frac{F_i^q(\delta q'_j) - F_j^q(-\delta q'_j)}{2\delta q'_j} \quad (11)$$

where the mass matrix $M = \sqrt{M_i M_j}$. To satisfy momentum conservation, K for $i = j$ (diagonal terms) is calculated from $K_{ii} = -\sum_{i \neq j} K_{ij}$. The angular frequencies of the vibrons (ω) can be calculated from the square root of the eigenvalues of the Dynamical Matrix. The wavefunction (φ) corresponding to the vibrational modes are the eigenvectors of the Dynamical Matrix D :

$$D\varphi = \omega^2 \varphi \quad (12)$$

The weight P_i of the wavefunction (φ) of the degree of freedom (q') on each modes i can be calculated as

$$P_i = \sum_{j \in q'} |\varphi_{ij}|^2 \quad (13)$$

The participation ratio of the modes associated with the center of mass motion on $x = [1 \ 0 \ 0]$, $y = [0 \ 1 \ 0]$ and $z = [0 \ 0 \ 1]$ directions can be calculated as:

$$R = \sqrt{Q_{x'}^2 + Q_{y'}^2 + Q_{z'}^2} \quad (14)$$

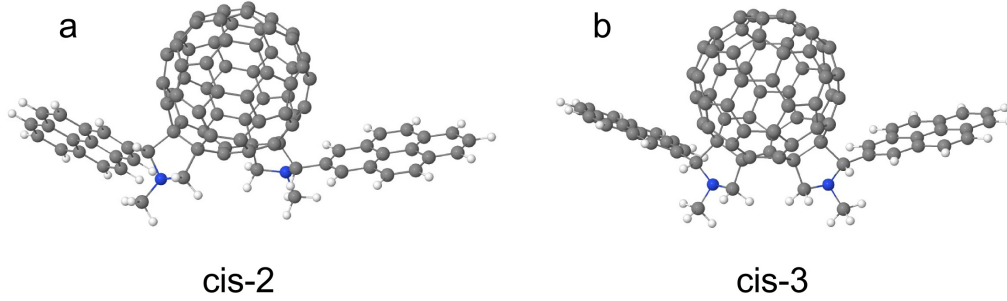


Figure S11: Molecular structure of bisadducts for two isomer cis-2 (a) and cis-3 (b) consisting of a C_{60} connected to two bis pyrene anchors.

where $Q_\beta = \langle \varphi | \beta \rangle / |\varphi| \sqrt{N}$ and $\beta = x', y', z'$. To study the behavior of the atoms in the time interval 0 to $t = n\pi$ due to a vibrational mode ω_i , the associated wavefunction φ_i is projected on x, y and z coordinate of the atoms as:

$$\hat{q}_i(t) = q_i + \frac{A}{M} \varphi_i \sin(t) \quad (15)$$

The $\hat{q}_i(t)$ are then recorded to make the animations as shown in the SI. The transport calculation is carried out using our implementation of the Greens function method, Gollum[11] with the same method as described in [12]. Also the iso-surfaces of the frontier orbitals has been computed with the same method as described in [12, 13, 14].

2.2 Molecular geometry

The molecular structures of the cis-2 and cis-3 isomers of bisadducts are shown in Figure S11. The geometry relaxation using DFT (see methods) shows that the bis pyrene anchors are not symmetric around the center of the central C_{60} . The angle between the anchors on the two side of C_{60} is higher for cis-2 isomer compared to cis-3.

2.3 Local density of states

Figure S12 shows the iso-surfaces of the frontier orbitals of the bisadducts. The wavefunctions are localized in the central C_{60} for LUMO levels whereas they are localized in both the central C_{60} and pyrene anchors for HOMO levels. This suggests HOMO dominated transport in this molecule. The DFT calculated KohnSham HOMO and LUMO energies are -4.41 and -3.07 for cis-2 and -4.59 and -3.12 for cis-3 isomer, respectively as shown in Table 1.

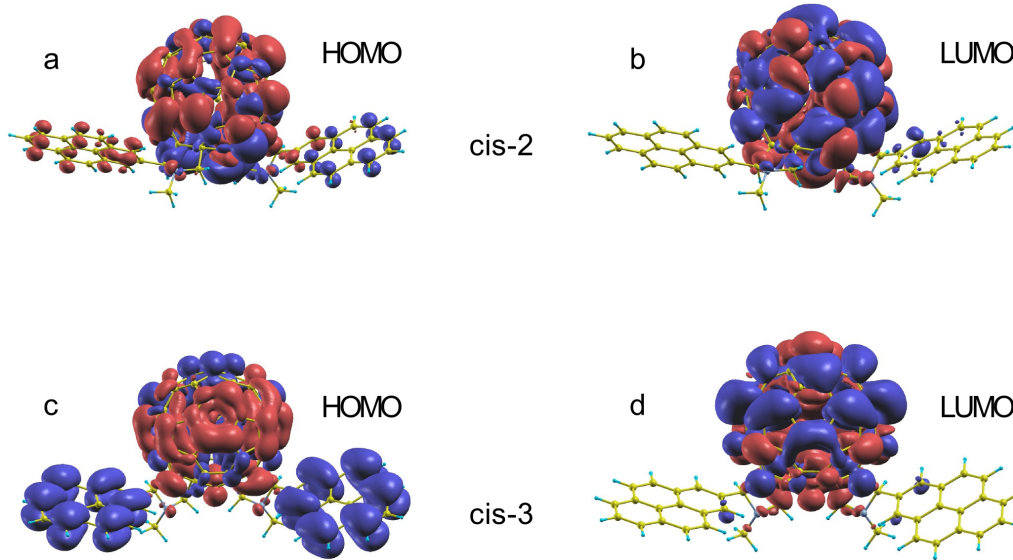


Figure S12: Iso-surfaces of the frontier orbitals of C_{60} bisadducts in gas phase. Local density of states of HOMO and LUMO level for cis-2 (a,b) and cis-3 (c,d) isomers.

| Level | cis-2 (eV) | cis-3 (eV) |
|----------------------|------------|------------|
| HOMO-2 | -4.71 | -4.69 |
| HOMO-1 | -4.64 | -4.60 |
| HOMO | -4.41 | -4.59 |
| LUMO | -3.07 | -3.12 |
| LUMO+1 | -3.05 | -2.86 |
| LUMO+2 | -2.76 | -2.86 |
| HOMO-LUMO Energy gap | 1.34 | 1.47 |

Table 1: The Kohn-Sham gap and energy levels around the Fermi energy.

2.4 Device geometry

For the cis-2 configuration, geometrical relaxation shows that the pyrene anchors of cis-2 isomer makes a planar structure with the graphene surface on one side but not the other due to the larger angle between the two anchors. In contrast, for the cis-3 configuration, the pyrene anchors makes a planar structure with the graphene surfaces on both sides. The distance between the pyrene anchors and graphene surface is 3.24 Å. The transport mechanism can be described by the interaction of wavefunctions localized in the π -orbitals of the graphene electrodes and the π -orbitals of the pyrene anchors.

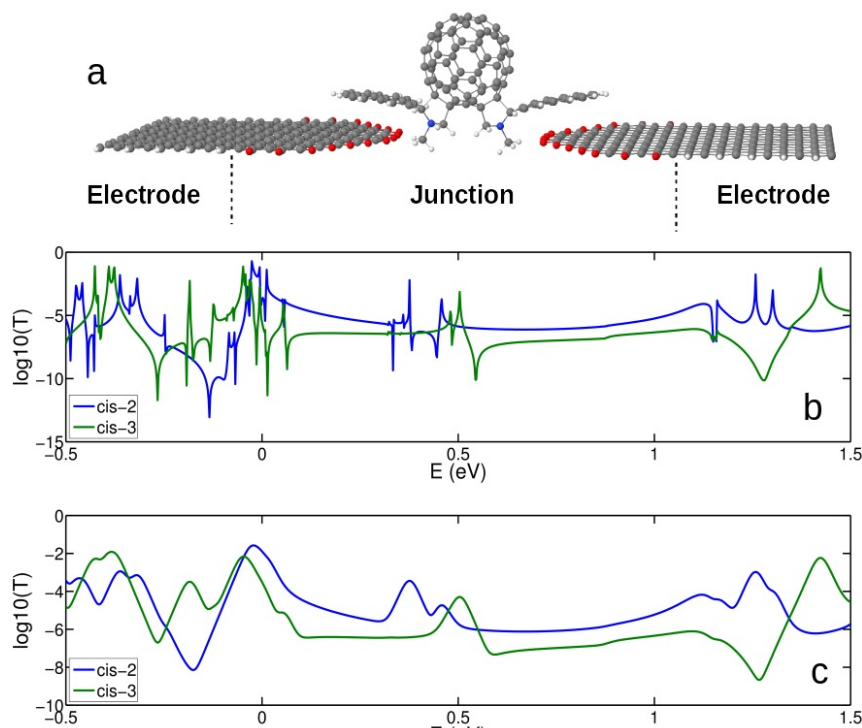


Figure S13: Electron transport through (a) graphene–bisadducts–graphene structure in (b) zero and (c) room temperature.

2.5 Electron transport

The electron transport is calculated with our implementation of NEGF method, Gollum (See methods). Figure S13 shows the transmission probability for the electrons with energy E passing from the left graphene electrode to the right through the π – π interaction with the bisadducts. The conductance through the cis-3 isomer (green curves) is predicted to be lower than cis-2 isomer (blue curves) around $E_F = 0$ eV. Consistent with LDOS calculations of the gas phase molecule, the HOMO resonance is close to the DFT predicted Fermi energy, suggesting HOMO dominated transport.

2.6 Vibrational modes of the cis-3 and cis-2 isomers.

The vibrational analysis of the cis-3 isomer is shown in Figure S14. Figure S14a is the analysis performed in the limit where the atomic mass of the pyrene anchor groups approach infinity. In this limit the anchor groups are effectively clamped and the modes corresponding to internal vibrations of the pyrene are filtered out of the vibrational spectrum. Red lines represent the total participation ratio while green corresponds to the participation ratio of modes associated

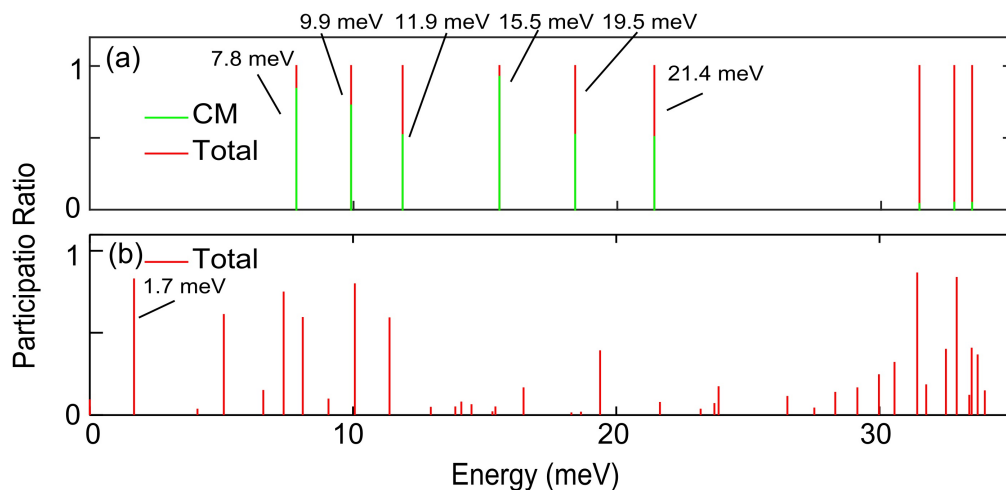


Figure S14: Vibrational analysis of bisadducts cis-3 isomer. (a) Atomic mass of pyrene groups approach infinity. (b) Normal mass.

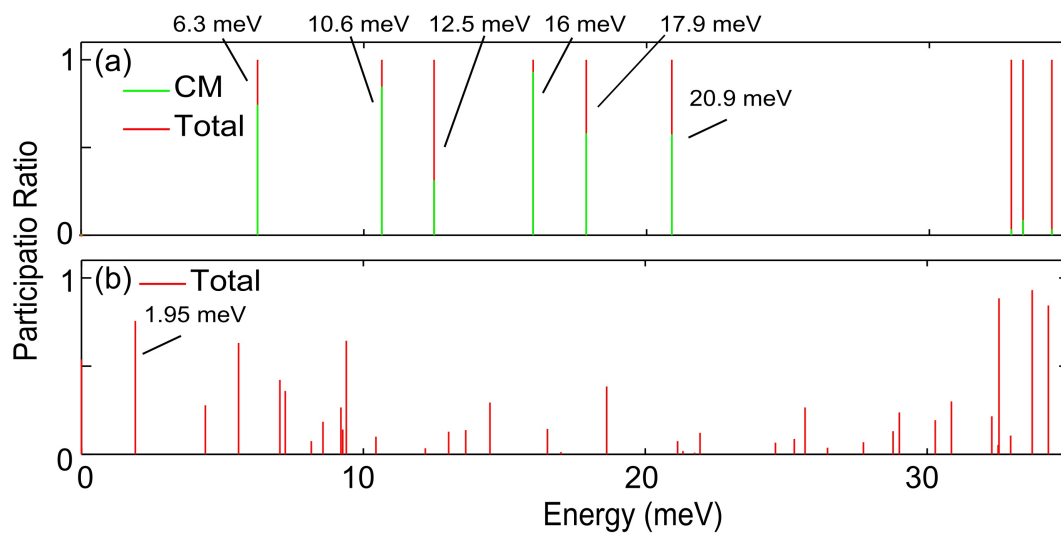


Figure S15: Vibrational analysis of bisadducts cis-2 isomer. (a) Atomic mass of pyrene groups approach infinity. (b) Normal mass.

with the center-of-mass motion. Figure S14b corresponds to the analysis performed using the normal mass for all atoms. The same vibrational analysis for cis-2 isomer is shown in Figure S15.

References

- [1] Kuzmany, H., Pfeiffer, R., Hulman, M. & Kramberger, C. Raman spectroscopy of fullerenes and fullerene-nanotube composites. *Philosophical Transactions of the Royal Society of London A: Mathematical, Physical and Engineering Sciences* **362**, 2375–2406 (2004).
- [2] Martin, M. C., Koller, D., Rosenberg, A., Kendziora, C. & Mihaly, L. Infrared and Raman evidence for dimers and polymers in RbC_{60} . *Physical Review B* **51**, 3210–3213 (1995).
- [3] Koch, J., Von Oppen, F., Oreg, Y. & Sela, E. Thermopower of single-molecule devices. *Physical Review B* **70**, 1–12 (2004).
- [4] Koch, J. & Von Oppen, F. Franck–Condon blockade and giant Fano factors in transport through single molecules. *Physical Review Letters* **94** (2005).
- [5] van der Heijden, J. *et al.* Probing the spin states of a single acceptor atom. *Nano Letters* **14**, 1492–1496 (2014).
- [6] Foxman, E., McEuen, P. & Meirav, U. Effects of quantum levels on transport through a Coulomb island. *Physical Review B* **47**, 20–23 (1993).
- [7] Leturcq, R. *et al.* Franck-condon blockade in suspended carbon nanotube quantum dots. *Nature Physics* **5**, 327–331 (2009).
- [8] Onac, E., Balestro, F., Trauzettel, B., Lodewijk, C. & Kouwenhoven, L. Shot-noise detection in a carbon nanotube quantum dot. *Physical Review Letters* **96**, 026803 (2006).
- [9] Sukhorukov, E. V., Burkard, G. & Loss, D. Noise of a Quantum-Dot System in the Co-tunneling Regime **63**, 20 (2000).
- [10] Greenfeld, M., Pavlichin, D. S., Mabuchi, H. & Herschlag, D. Single molecule analysis research tool (smart): An integrated approach for analyzing single molecule data. *PLoS ONE* **7** (2012).
- [11] Ferrer, J. *et al.* GOLLUM: a next-generation simulation tool for electron, thermal and spin transport. *New Journal of Physics* **16**, 093029 (2014).
- [12] Sadeghi, H. *et al.* Conductance enlargement in picoscale electroburnt graphene nanojunctions. *Proceedings of the National Academy of Sciences* **112**, 2658–2663 (2015).
- [13] Geng, Y. *et al.* Magic Ratios for Connectivity–Driven Electrical Conductance of Graphene-like Molecules. *Journal of the American Chemical Society* **137**, 4469–4476 (2015).

- [14] Al-Galiby, Q., Grace, I., Sadeghi, H. & Lambert, C. J. Exploiting the extended π -system of perylene bisimide for label-free single-molecule sensing. *Journal of Materials Chemistry C* **3**, 2101–2106 (2015).